Article

Effect of Al-Si Coating on the Interfacial Microstructure and Corrosion Resistance of Dissimilar Laser Al Alloy/22MnB5 Steel Joints

Lingqing Wu [1], Joao Pedro Oliveira [2], Jin Yang [1,*], Ming Xiao [1], Min Zheng [3], Wenhu Xu [1], Yixuan Zhao [1,*], Feifan Wang [4] and Hua Zhang [1,3]

[1] School of Materials Engineering, Shanghai University of Engineering Science, Shanghai 201620, China
[2] CENIMAT|i3N, Department of Materials Science, School of Science and Technology, NOVA University Lisbon, 2829-516 Caparica, Portugal
[3] School of Advanced Manufacturing, Nanchang University, Nanchang 330031, China
[4] Beijing Institute of Astronautical Systems Engineering, Beijing 100076, China
* Correspondence: jyang@sues.edu.cn (J.Y.); zhaoyx92@163.com (Y.Z.)

Abstract: This investigation employed different laser powers to conduct the laser welding–brazing process of 5052 aluminum alloy to both Al-Si coated and uncoated 22MnB5 steel. The flux-cored Zn-Al22 filler metal was employed during the procedure. The influence of Al-Si coatings on the microstructure and corrosion resistance of Al/Steel welded joints was investigated using microstructural characterization and electrochemical tests. It was noted that the interfacial microstructure of the laser Al/steel joints was significantly altered by the Al-Si coating. Moreover, the Al-Si coating suppressed the formation and growth of the interfacial reaction layer. Electrochemical corrosion tests showed that the impact of Al-Si coating on the corrosion resistance of laser joints depended on the laser powers and thickness of the interfacial intermetallic compound (IMC) layer. The research suggests that galvanic corrosion occurs due to the differences in corrosion potential between fusion zone (FZ), steel, and Fe-Al-Zn IMCs, which accelerate the corrosion of the joint. The IMC layer acts as a cathode to accelerate the corrosion of the FZ and as an anode to protect the steel from corrosion.

Keywords: corrosion resistance; laser welding–brazing; intermetallic compounds; microstructure; Al/steel joints

1. Introduction

Lightweight design and manufacturing of automotive structures are fundamental for the development of the motor industry [1–3]. Due to the advantages of being lightweight and exceptionally resistant to corrosion, aluminum alloys have good prospects for application in the weight reduction of automotive structures by replacing conventionally used steels [4–6]. At the same time, to satisfy the demand for weight reduction and to improve the safety and crashworthiness qualities of vehicles, automakers have made remarkable advancements in the production of sophisticated high-strength steels (AHSSs), including martensitic steel, dual-phase steel, and boron alloy steel to obtain higher strength and thinner structural sizes [7]. The AHSSs have a higher strength than conventional mild steels but have poor formability. The 22MnB5 is a boron-containing alloy steel. It has a completely martensitic microstructure and offers unparalleled strength compared to the AHSS currently employed in the industry. In order to eliminate the disadvantage of low-formation properties, 22MnB5 steel is formed by a hot-forming process, so it was called a hot stamping steel. The 22MnB5 steel shows a high ultimate tensile strength after hot stamping [8,9].

Extensive research has been conducted to investigate different types of coatings, including Al-Si and Zn coatings, to mitigate surface oxidation that may occur during high-temperature procedures [10]. The Al-Si coatings leave no oxide stripping during heating on

the steel surface, can be dispensed with shot blasting or sand blasting after stamping, and possess a high corrosion resistance without nitrogen protection. Therefore, Al-Si coatings have been more widely used in hot stamping and forming processes than Zn coating. It was inevitable that scholars would consider the influence of Al-Si coating during the welding process. A study conducted by Kim et al. [9] aimed to examine the effects of Al-Si coating in laser welding on 22MnB5 steel (Martin Steel Inc., Huntington, WV, USA). The researchers discovered that, when an Al-Si coating was present, the aluminum and silicon elements dissolved into the weld. These elements primarily formed a solid solution within the weld. Furthermore, the aluminum and silicon precipitated on the interface, leading to a weak joint strength. Sun et al. [11] focused on the effect of Al-Si coating on the joint strength of steel joints. According to this investigation, the ferrite generated by Al-Si coating exhibits a low hardness and strength. It is beneficial for enhancing the joint's fatigue life. Lin et al. [12] observed an increase in the aluminum content in the fusion zone (FZ) of 22MnB5 steel joints as a result of the Al-Si coating dissolving. Furthermore, aluminum promoted the generation of δ-Fe during solidification, which weakened the joint's mechanical properties. In the case of dissimilar welding, Ding et al. [13] proposed to join Al/Al-Si coated steel by refill friction stir spot welding and found that the Al_5Fe_2 (Si) existing in the Al-Si coating can inhibit the formation of IMC in the joint. Zhang et al. [14] welded magnesium and Al-Si coated 22MnB5 steels by resistance spot welding. They investigated the impact of the Al-Si coating on the strength and microstructure of the joints. It was demonstrated that the molten Al-Si eutectic promoted the evolution of the reaction, generating a new IMC layer in the center of the weld, which significantly improved the mechanical properties of the joint. There are many welding methods for dissimilar metals, such as friction stir welding [15], explosion welding [16], gas tungsten arc welding (GTAW) [17], and laser welding [18,19]. The advantages of laser welding are a high energy density, concentrated energy, easy control of the heat source, deep weld seam, small welding deformation, and high efficiency, which are promising for aluminum/steel dissimilar welding [20–22]. Yang et al. [19] studied the association between laser power, interfacial microstructure, and joint strength of Al/Al-Si coated 22MnB5 steel joints. The results of the study demonstrated significant variations in the type and structure of intermetallic compounds (IMCs) within the interfacial layer under different laser power conditions. These findings emphasize the effect of laser power on the formation and characteristics of IMCs.

Based on the above literature, it can be summarized that Al-Si coatings have a significant impact on the microstructure and mechanical properties of welds. However, there is still little literature on the effect of Al-Si coatings on the corrosion resistance of dissimilar Al/steel joints. Al-Si coating can improve the corrosion resistance of 22MnB5 steel surface, but the impact on the corrosion resistance of Al/steel dissimilar joints is unclear. Corrosion between Al/steel dissimilar joints is more prone to occur, which is caused by the difference in self-corrosion potential between the two materials. Hence, investigating the effect of Al-Si coating on the corrosion resistance of Al/22MnB5 steel joints is necessary. In the present study, the interfacial microstructure was comparatively analyzed in Al/22MnB5 steel joints with and without Al-Si coating. In order to study the effect of coatings on the corrosion resistance of the joints, self-corrosion current density, self-corrosion potential, and impedance of Al-steel joints were measured by electrochemical tests. The morphology of the joints after corrosion was analyzed, and illustrated the corrosion mechanism of the Al/steel joints. This will provide theoretical support for enhancing the security and stability of Al/steel welded construction products in the manufacturing industry.

2. Experimental Design

The thickness of the base metals, AA5052 aluminum alloy (Guangdong Xingfa Aluminium Co., Ltd., Guangdong, China) and 22MnB5 steel (with or without Al-Si coating), used in this experiment were 2.0 mm and 1.8 mm, respectively. These base metals had dimensions of 100 mm × 50 mm. For this experiment, the Zn-Al22 wire was chosen as the filler metal, which had a diameter of 1.6 mm. Table 1 provides the elemental content of

the the22MnB5 steel (Baosteel Co., Ltd., Shanghai, China), AA5052 aluminum alloy, and Zn-Al22 filler wire (Shandong Szeshang Welding Materials Co., Ltd., Shandong, China). Figure 1 shows the microstructure of the 22MnB5 steel with and without coating. In terms of uncoated steel, pearlite and ferrite were observed (Figure 1a), while only martensite was observed due to the hot stamping process inducing phase transformation [14]. In addition, the Al-Si coating with the thickness of 28 ± 2 µm was clearly observed on the steel substrate (Figure 1b). This coating consisted of an Al-Si eutectic phase and Fe_2Al_7Si intermetallic compound, where the IMCs were continuously distributed between the Al-Si eutectic phase and steel substrate with the thickness of 7 µm [23–25].

Table 1. Chemical composition of base metals and filler metal (wt. %).

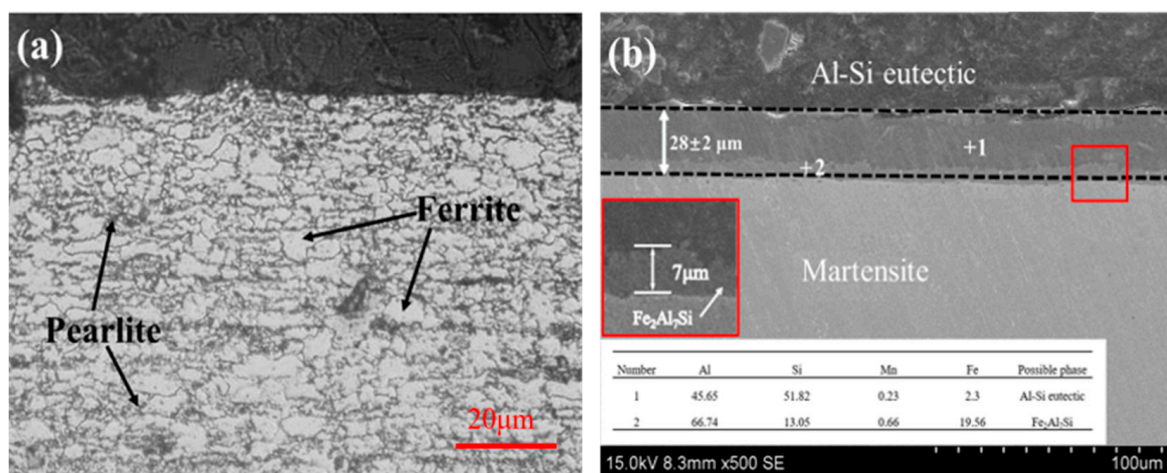| Materials	Mg	Fe	Al	Cr	Cu	Zn	Mn	Si	C	B
22MnB5 steel	-	Bal.	0.05	0.20	-	-	1.18	0.25	0.2	0.005
AA5052 Al	2.2–2.8	0.4	Bal.	0.2	0.1	0.1	0.1	0.25	-	-
Zn-Al22	-	-	22	-	0.8	Bal.	-	-	-	-

Figure 1. Microstructure of 22MnB5 steel: (**a**) without coating; (**b**) with coating.

The IPG YLS-5000 fiber laser system (IPG Photonics, Oxford, MA, USA), capable of producing a maximum output power of 5 kW, was utilized to conduct the welding procedure. A visual representation of the Al/steel laser welding–brazing process can be observed in Figure 2. To ensure the cleanliness of the workpieces, the base metal was wiped with ethanol after being smoothed by sandpaper to remove scraps and oils before welding. The welding joint determined the lap joint, the steel was placed on the bottom of aluminum, and the width of the overlap was 10 mm. The filler metal was fed from the front of the laser beam at an angle of 45°. The angle between the laser beam and the workpiece was approximately 90°. The filler metal was fed from the front of the laser beam at an angle of 45°. A total of 99.99% pure Ar shielding gas was used to prevent oxidation during welding with a flow rate of 15 L/min. The angle between the workpiece and the protective gas feed nozzle was set at 30°. In order to obtain a wider laser irradiation area, the laser defocus parameter can be set to +35 mm. To obtain a satisfactory weld appearance, the experimental parameters need to be optimized before the beginning of the test. Table 2 shows the optimized parameters for the dissimilar laser welding–brazing.
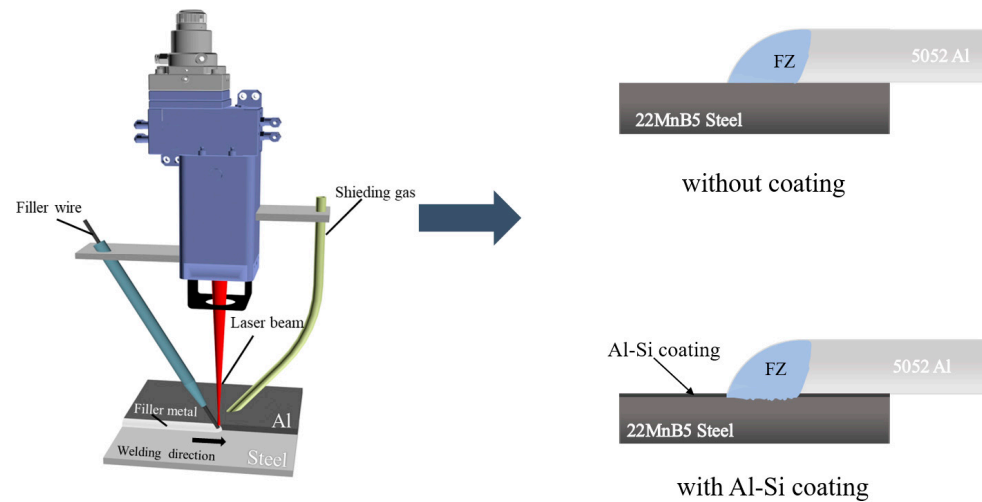
Figure 2. Schematic diagrams of laser welding–brazing of Al/steel.

Table 2. Optimized parameters of laser welding–brazing.

Laser Power /W	Welding Speed /m·min^{-1}	Wired Feed Speed /m·min^{-1}	Defocused Amount /mm	Shielding Gas Flow /L·min^{-1}
1500 1700 1900	0.3	1.9	+35	15

After welding, the laser joints were cut along the direction perpendicular to the laser movement and subjected to microstructure analysis. The samples were sequentially ground with 400#, 800#, 1200#, and 1500# metallographic sandpapers for coarse and fine grinding, and polished with 1 μm diamond suspension until becoming scratch-free. Then, metallographic specimens were ultrasonically cleaned in acetone. The welding samples were observed using an optical microscope (OM, Olympus 4XCJZ, Olympus Group, Milwaukee, WI, USA) and scanning electron microscope (SEM, Hitachi S3400-N, ATA Scientific Pty Ltd., Caringbah, Australia) in order to analyze the microstructure and ascertain the chemical composition of the interfacial phases. The scanning electron microscope was also equipped with energy-dispersive X-ray spectroscopy (EDS, Nogales, AZ, USA) analysis for further investigation.

A CS350H electrochemical workstation (Wuhan Corrtest Instruments, Wuhan, China) and three-electrode system were used for the electrochemical corrosion testing, as shown in Figure 3. The saturated calomel electrode was used as the reference electrode. The electrochemical corrosion sample was used as the working electrode, and the platinum electrode was used as the counter electrode. A neutral solution of 0.35 mol/L NaCl was used in the electrochemical corrosion. In the electrochemical corrosion test, except for the polished cross-section, the rest of the material was covered with epoxy resin, and only the cross-section of the sample was retained as the surface to be tested. The samples were immersed in the NaCl neutral solution for 30 min to obtain uniform corrosion. After the open-circuit potential (OCP) became stabilized, the potential dynamic polarization curve test scanned from negative potential to positive potential, and the applied potential varied in the range of −1.5 to +1 V. The scan speed and sampling frequency during the test were 2 mV/s and 2 Hz, respectively. The electrochemical impedance spectroscopy (EIS) was conducted when the open-circuit potential is relatively stable, with the amplitude of the sinusoidal voltage set to 10 mV and the frequency set to 1000 to 0.1 Hz.
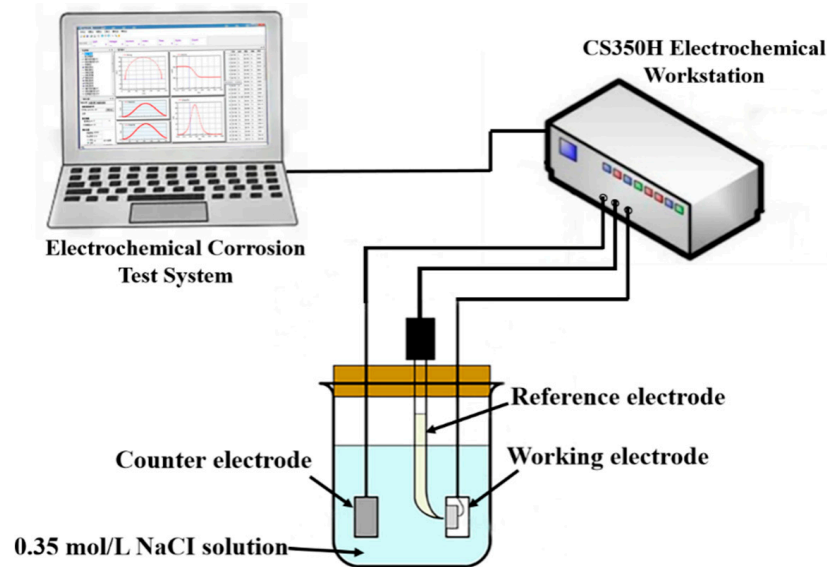
Figure 3. Schematic diagram of electrochemical corrosion test.

3. Results and Discussion

3.1. Macroscopic Morphology and Interfacial Microstructure

Figure 4 shows the macroscopic morphology of welding joints with and without Al-Si coating. It was evident that the welding joints were continuous and well-formed, with no visible surface defects such as spatter or porosity. The width of the filler metal on both uncoated and Al-Si coated steel increased gradually with increasing laser power, indicating that the heat input improved the wetting and spreading of the filler metal.
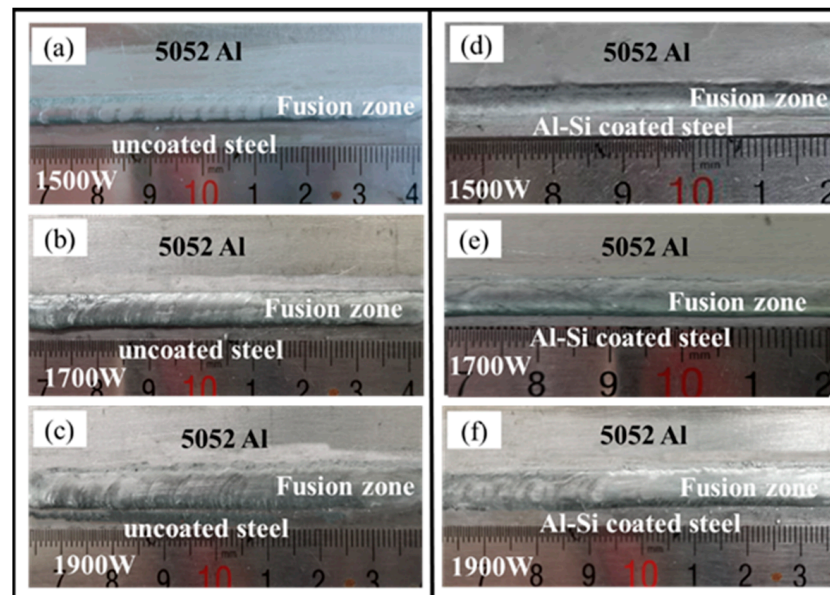

Figure 4. Macroscopic morphology of welding joints with the laser power from 1500 W to 1900 W: (**a**–**c**) Al/uncoated steel joints; (**d**–**f**) Al/Al-Si coated steel joints.

Figure 5 shows the SEM analysis at the FZ/steel interface of the laser joints with and without Al-Si coating obtained with various laser powers. It was obvious that the reaction layer was generated at the interface under both conditions.
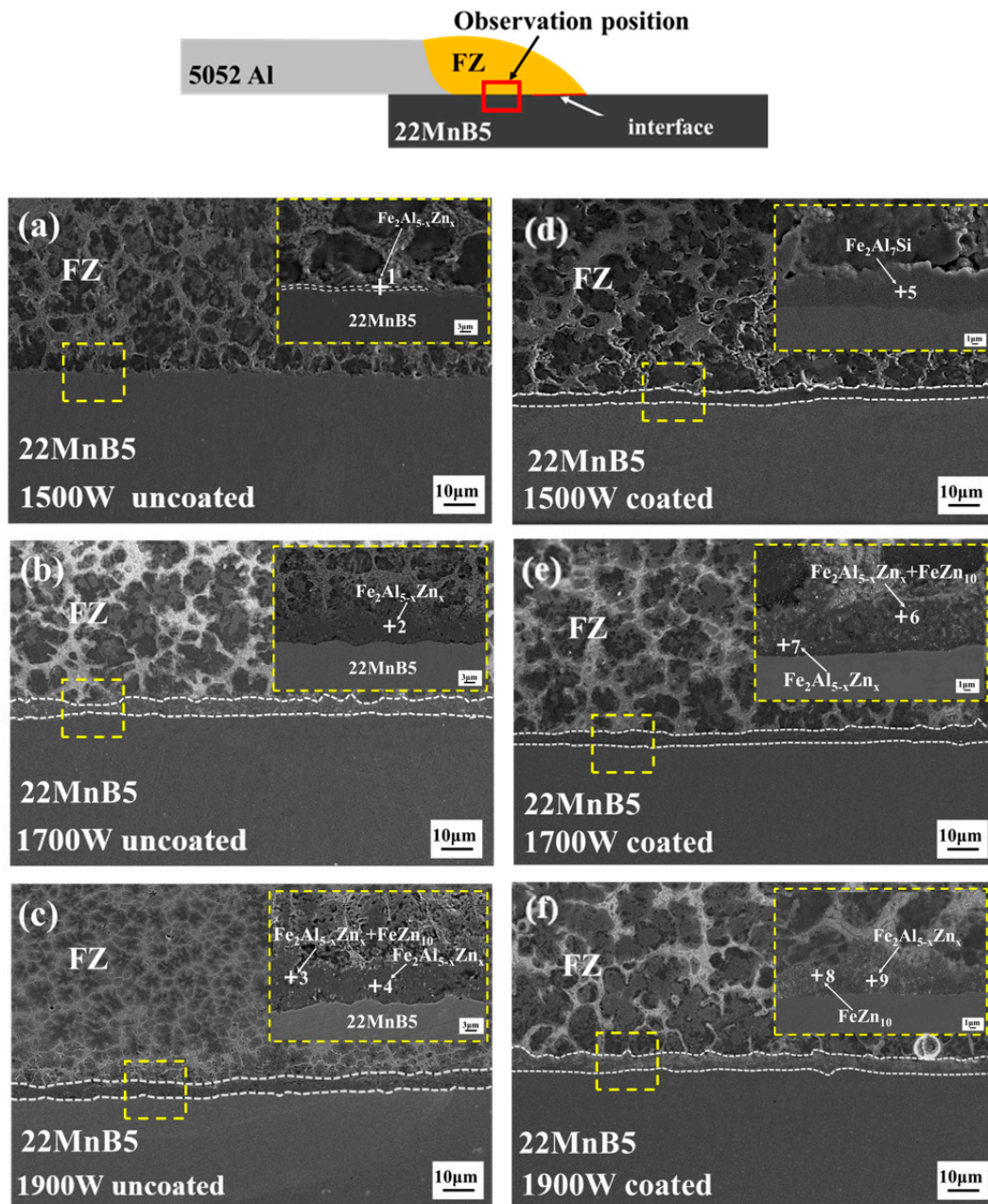
Figure 5. SEM analysis at the FZ/steel interface in the Al/uncoated steel and Al/Al-Si coated steel joints with the laser power varying from 1500 to 1900 W: (**a~c**) Al/uncoated steel joints; (**d~f**) Al/Al-Si coated steel joints.

Figure 5a–c depicts the SEM analysis of the laser Al/uncoated steel joints. In the case of the uncoated steel, the morphology and phase composition of the reaction layer changed drastically from 1500 to 1900 W (refer to Figure 5a–c). At the low laser power of 1500 W, the reaction layer was very thin and discontinuous, and the edge of the reaction layer close to the steel base metal was relatively straight, while it was uneven near the FZ. This indicates that the reaction layer has grown from the steel side towards the FZ [26]. According to the EDS analysis in Table 3, the chemical composition was 0.82 at. % Fe, 48.89 at. % Al, 50.11 at. % Zn, and 0.18 at. % Si. These measurements indicated that existing phases were mainly $Fe_2Al_{5-x}Zn_x$. The $Fe_2Al_{5-x}Zn_x$ was a kind of variation of Fe_2Al_5 which has been reported previously [27]. A thicker reaction layer was observed consisting of a continuous dark lamellar layer at 1700 W. According to EDS analysis in Table 3, the chemical composition was 23.10 at. % Fe, 70.24 at. % Al, 60.42 at. % Zn, and 0.24 at. % Si, which was determined to

be $Fe_2Al_{5-x}Zn_x$ [28,29]. Upon increasing the laser power to 1900 W, a continuous reaction layer was observed, which comprised a thicker dark layer with dispersed light-colored microstructure. The elemental composition and content of the two phases was 11.46 at. % Fe, 57.41 at. % Al, 31.04 at. % Zn, 0.09 at. % Si and 19.58 at. % Fe, 70.6 at. % Al, 9.62 at. % Zn, 0.21 at. % Si (Table 3). The existing phases were determined to be $Fe_2Al_{5-x}Zn_x$ and $FeZn_{10}$. Similar phase determinations have also been reported in a related investigation [30–32].

Table 3. EDS results in selected regions in Figure 5.

Points	Elements (at. %)				Possible Phases
	Al	**Fe**	**Zn**	**Si**	
1	48.89	0.82	50.11	0.18	$Fe_2Al_{5-x}Zn_x$
2	70.24	23.10	6.42	0.24	$Fe_2Al_{5-x}Zn_x$
3	57.41	11.46	31.04	0.09	$Fe_2Al_{5-x}Zn_x + FeZn_{10}$
4	70.6	19.58	9.62	0.21	$Fe_2Al_{5-x}Zn_x$
5	68.75	17.00	1.95	12.30	Fe_2Al_7Si
6	54.81	16.26	26.01	2.92	$Fe_2Al_{5-x}Zn_x + FeZn_{10}$
7	63.67	19.94	10.48	5.92	$Fe_2Al_{5-x}Zn_x$
8	67.92	20.68	7.23	4.16	$Fe_2Al_{5-x}Zn_x$
9	16.01	11.74	71.89	0.35	$Fe_2Al_{5-x}Zn_x + FeZn_{10}$

Figure 5d–f shows the SEM analysis of laser Al/Al-Si coated steel joints. At the low laser power of 1500 W, a relatively flat reaction layer at the interface was found, consisting of a dense dark phase as shown in Figure 5d. Through the process of analysis, the main element of the dark phase was Al, with some Fe and Si and a small amount of Zn, which was determined to be Fe_2Al_7Si (Table 3). In fact, Fe_2Al_7Si was the IMC phase that pre-existed in the Al-Si coating (Figure 1b), which indicated that the laser heat input was insufficient to melt the IMCs where only dissolution was expected to occur. At the medium laser power of 1700 W, a continuous reaction layer was also present. However, the difference was that a small amount of light-colored microstructure was within the dark reaction layer as shown in Figure 5e. According to the results of EDS, the dark phase consists mainly of iron, aluminum, and zinc elements, which were determined to be $Fe_2Al_{5-x}Zn_x$. By analyzing the elemental composition and content of the light-color phase, it was indicated that the phase mainly consisted of $FeZn_{10}$. This suggests that the compounds in the coating melted and generated new IMCs. Upon increasing the laser power to 1900 W, a dark phase and a light-color dispersion phase were observed at the interface. In the local area, the light-color phase was observed, which was irregularly distributed in the dark phase (Figure 5f). Through the process of analysis of the EDS results, the dark phase and the light-color phase were determined to be $Fe_2Al_{5-x}Zn_x$ and $FeZn_{10}$, respectively (refer to Table 3). Therefore, it was concluded that the Al-Si coating was completely melted or dissolved in the laser powers from 1700 to 1900 W, where new phases were then generated at the interface.

Except for the phase composition, the morphological characteristics of the interfacial intermetallic compound (IMC) layer changed significantly. In order to better understand this, a quantitative analysis was conducted on the change of the interfacial reaction layer. The thickness of the IMCs in both cases with the laser power range from 1500 to 1900 W is shown in Table 4. Due to an elevated temperature, an intensified diffusion reaction occurred at the interface, which led to an increase in intermetallic compound thickness with the rise in laser power [33]. The intermetallic compound thickness in the joint of Al/coated steel was larger as compared to the joint of Al/uncoated steel (7.1 μm vs. 1.5 μm) at 1500 W. This was because the interfacial metallurgical reactions were relatively weak at low laser power, only generating a 1.5 μm thick IMC layer which was much thinner than the pre-existed 7 μm thick Fe_2Al_7Si layer within the Al-Si coating. The thickness of the IMCs of the Al/Al-Si coated steel joints was thicker than that of the Al/uncoated steel joints with the laser power rising from 1700 to 1900 W (Table 4). This was primarily attributed to the Al-Si coating of 22MnB5 steel acted as a thermal and diffusion barrier between the

molten pool and steel substrate that retarded the growth of the reaction layer [7,11]. It was suggested that the Al-Si coating was able to effectively suppress the formation and growth of interfacial IMCs.

Table 4. The thickness of IMC of the laser joints with a different laser power in both cases (μm).

Cases	1500 W	1700 W	1900 W
Al/Al-Si coated steel joints	7.1	8.2	10.3
Al/uncoated steel joints	1.5	11.1	16.6

3.2. Corrosion Resistance

3.2.1. Open-Circuit Potential

In order to accurately measure the voltage sweep range of the specimen's polarization curve, it is necessary to identify the open-circuit potential (OCP) and thus determine the voltage sweep range [17]. The open-circuit potential is the difference between the working electrode and the reference electrode without load, which is mainly related to the material and the corrosive solution. The change in the OCP reflects the gradual transformation of the electrode from an unstable to a stable state in the electrolyte solution.

Figure 6 shows the OCP curves of base materials and laser joints. The OCP of the Al base metal was −0.74 V, with slight fluctuations due to the generation and breakdown of the passivation film on the aluminum alloy surface during the corrosion process [34]. The OCP of the Al-Si coated steel was −0.65 V, which was significantly higher than the uncoated steel (−0.72 V). It was indicated that the Al-Si coating increased the potential and reduced corrosion tendency on the steel surface. Figure 6b shows the OCP curves of the laser joints at different laser powers. Certain fluctuations were observed in all the OCP curves, due to the corrosion dissolution of the interfacial IMC layer. With the increase in the laser power from 1500 to 1900 W, the steady-state OCPs of Al/uncoated steel joints were −0.849 V, −0.830 V, and −0.884 V. The steady-state OCPs of Al/Al-Si coated steel joints were −0.827 V, −0.832 V, and −0.860 V. As a whole, it was concluded that the Al/uncoated steel joint exhibits a slightly lower steady-state OCP in comparison to the Al/Al-Si coated steel joint at the same laser power.
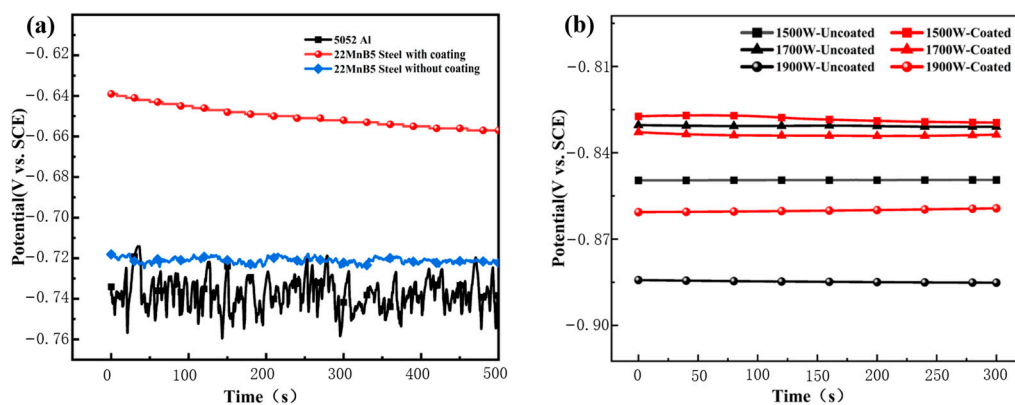

Figure 6. Open-circuit potential curves: (**a**) base metals; (**b**) Al/Al-Si coated and uncoated steel joints.

3.2.2. Dynamic Potential Polarization

Figure 7 depicts a schematic diagram of the kinetic potential polarization curve of a typical laser Al/steel joint. The dynamic potential polarization curve consists of a cathodic semi-log polarization curve and an anodic semi-log polarization curve, where the intersection of the two polarization potential curves is the self-corrosion potential, *Ecorr*. *Ecorr* represents the stable corrosion state of the potential in the absence of an applied current; to some extent, it is also a thermodynamic parameter that reflects the corrosion tendency of the joint. The relatively small *Ecorr* indicates that the joint in the natural state

is more prone to corrosion. The self-corrosion potential, *Ecorr*, only reflects the corrosion trend, and there is no certain relationship with the corrosion rate [35].
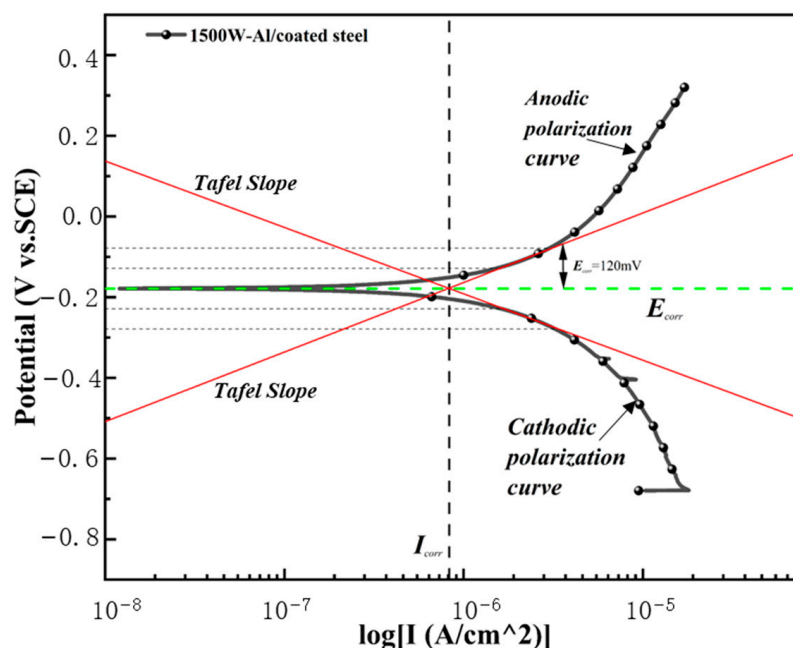

Figure 7. Dynamic potential polarization curve of a typical laser Al/Al-Si coated steel joint.

The Tafel extrapolation method was used to fit the strongly polarized region of the polarization curve (the position where the polarization potential deviates far enough from the self-corrosion potential) to obtain the intersection of two Tafel curves. The value of the horizontal coordinate corresponding to the intersection was lg(*icorr*), which is the self-corrosion current density. The self-corrosion current density *icorr* is typically used to indicate the corrosion rate in electrochemical corrosion. In the natural state, the corrosion rate of the joint increases as the *icorr* value becomes larger. The polarization potential as a function of the applied polarization current density was in accordance with the Tafel equation:

$$E - Ecorr = -balgicorr + balgia \tag{1}$$

$$Ecorr - E = -bclgicorr + bclgic \tag{2}$$

where, E is the polarization potential, *Ecorr* is the self-corrosion potential, *icorr* is the self-corrosion current density, b_a, and b_c are the anodic and cathodic Tafel slopes, and i_a and i_c are the anodic and cathodic corrosion current densities.

Figure 8 depicts the comparative analysis of the dynamic potential polarization curves of the laser Al/steel joints. The dynamic potential polarization curves of the joints with and without coating were both very smooth and followed a similar trend, i.e., initially, the current density decreased as the potential increased, but then rose again. To further investigate the influence of the coating on the corrosion resistance of the joints, the Tafel recursive method was used to calculate the self-corrosion current density and self-corrosion potential as shown in Table 5. It can be concluded that the self-corrosion potential of the Al/Steel laser joints varied little with the increase in laser power, but the self-corrosion current density gradually increased. At the same time, the addition of Al-Si coating decreases the self-corrosion current density of the Al joints. This indicated that the increase in laser power decreases the corrosion resistance of the joints and the Al-Si coating improves the corrosion resistance of the joints.
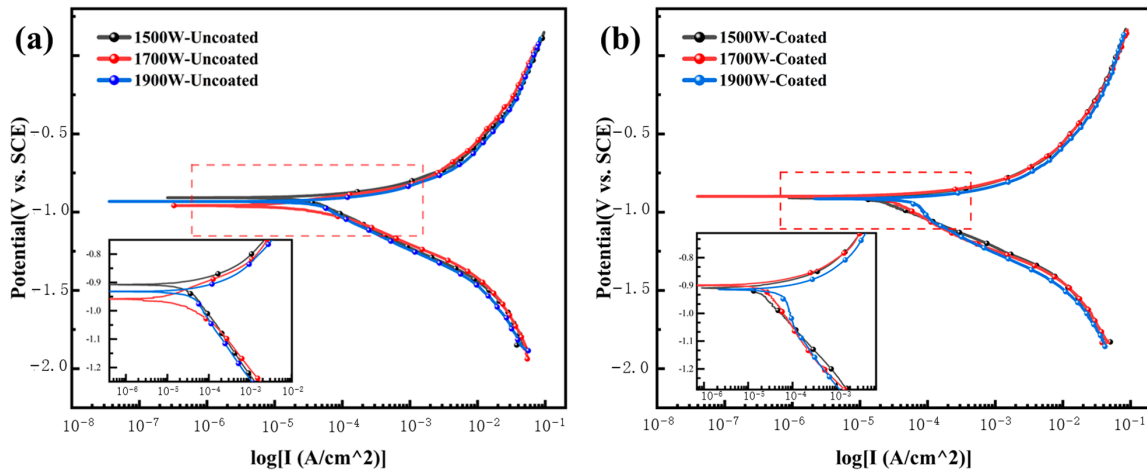
Figure 8. Potential dynamic polarization curves: (**a**) Al/uncoated steel joints; (**b**) Al/Al-Si coated steel joints.

Figure 9 details the self-corrosion current density with the change in power for the Al/steel welded joints with or without coating. With the increased laser power, the self-corrosion current density of Al/uncoated steel were 2.02×10^{-5} A/cm^2, 5.72×10^{-5} A/cm^2, and 7.47×10^{-5} A/cm^2, and the self-corrosion current density of Al/Al-Si coated steel were 3.35×10^{-5} A/cm^2, 3.83×10^{-5} A/cm^2, and 6.22×10^{-5} A/cm^2. It was obvious that the self-corrosion current density of both joints increased with the increase in laser power, which further indicated that increasing the laser power was likely to reduce the corrosion resistance of the joints. By comparing the self-corrosion current density under the same power, opposite trends were observed for various laser powers. The self-corrosion current density of the laser Al/Al-Si coated steel joints were higher as compared to the joints of Al/uncoated steel (3.35×10^{-5} A/cm^2 vs. 2.02×10^{-5} A/cm^2) at 1500 W. On the contrary, at a laser power of 1700 and 1900 W, the self-corrosion current density of the Al/uncoated steel joints was greater as compared to the Al/Al-Si coated steel joints. Combining the effects of laser power and steel surface condition on the IMC thickness, there was evidence of a high correlation between the IMC thickness and self-corrosion current density in Figure 9. Therefore, according to the findings, interface intermetallic compound thickness and subsequently the corrosion properties of the laser joints were influenced by both the laser power and coating [36,37]. In a word, the thinner the IMC layer, the lower the self-corrosion current density, and the better joint corrosion performance.
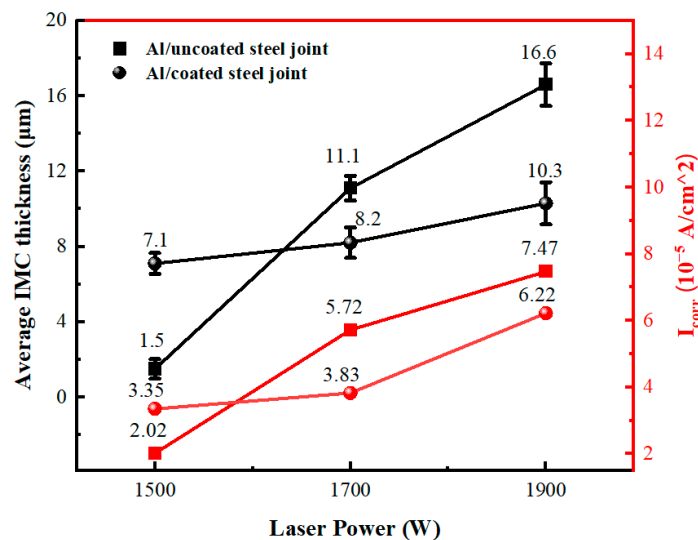

Figure 9. Average IMC thickness and self-corrosion current density of joints with different laser powers.

Table 5. Self-corrosion potential and self-corrosion current density of Al/Steel joints.

Laser Power (W)	Corrosion Current Density (10^{-5} A/cm^2)		Corrosion Potential (V)	
	Uncoated Steel	Coated Steel	Uncoated Steel	Coated Steel
1500 W	2.0235	3.3538	−0.945	−0.9683
1700 W	5.7234	3.8333	−0.9512	−0.952
1900 W	7.4773	6.2223	−0.9637	−0.9854

3.2.3. Electrochemical Impedance Spectroscopy

Electrochemical impedance spectroscopy (EIS) is usually used to characterize the charge transfer and substance transport processes during corrosion. Figure 10a shows the Nyquist plots of Al/Al-Si coated and Al/uncoated steel joints with laser power from 1500 to 1900 W. The radius of the semicircle decreased with increasing laser power in both cases of joints, which indicated a reduction in the corrosion resistance of the joints. At a laser power of 1500 W, the semicircle radius of Al/uncoated steel joints was larger than that of Al/Al-Si coated steel joints; the opposite was true at high laser power (1700–1900 W). It was indicated that Al/Al-Si coated steel joints possess a higher corrosion resistance compared with Al/uncoated steel joints at a high laser power. This was possibly related to interfacial intermetallic compound thickness. Nyquist plots of the Al/uncoated steel laser joints showed one induction loop at laser powers of 1500 and 1700 W. The inductive resistance at a low frequency was mainly attributed to the absorption and desorption of the material or the formation of corrosion pits on the electrode surface [38]. The curve peak in the Bode plots was normally used to determine relaxation time (Figure 10b). During corrosion, the relaxation time reflected the charge transfer from instability to equilibrium [39]. All samples tested in this experiment showed a shift in the characteristic minimum frequency toward a high frequency with increasing laser power, indicating that more time was needed for re-passivation, which suggested a decrease in the corrosion resistance. According to the above results, it can be summarized that the corrosion resistance of laser joints decreased with the increased laser power, and Al-Si coating improved the corrosion resistance of the joints especially at high laser powers.
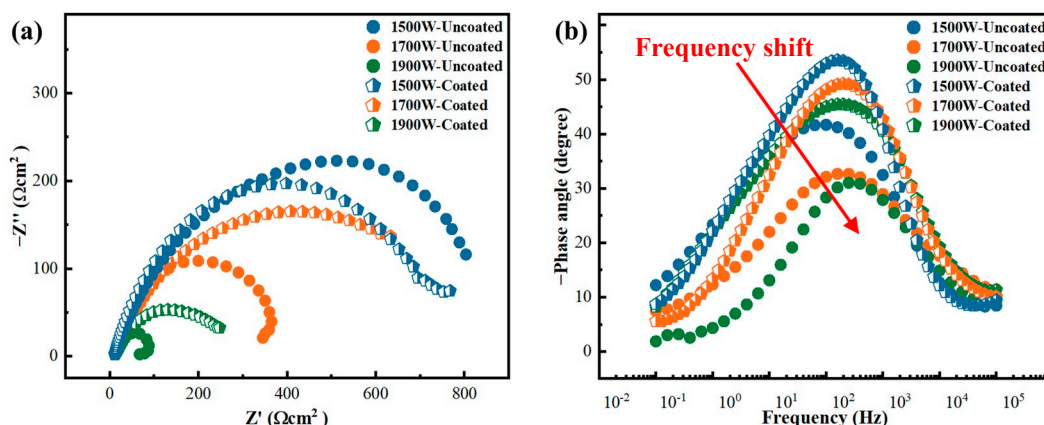
Figure 10. (**a**) Nyquist plots of laser Al/steel joints; (**b**) Bode plots of laser Al/steel joints.

3.2.4. Corrosion Morphology and Mechanism of Welded Joint

In order to further investigate the Al/steel welding joint corrosion mechanism, typical corrosion morphology at the interface of laser Al/coated steel joints at a laser power of 1900 W was observed (Figure 11). Figure 12 shows the schematic diagram of the corrosion mechanism of Al/steel welded joints in 3.5% NaCl solution. The corrosion pits were found on the steel surface, which was due to the reaction of Cl- with the hydroxide of Fe and the formation of complexes on the steel surface accelerating the pitting corrosion [40]. It

can be seen that there is a darker color in the FZ and a brighter color of the joint steel side in Figure 11b. This indicates that the FZ corrodes more severely than the steel. This was because the galvanic corrosion occurred between the FZ and the steel, where the FZ with a lower corrosion potential exhibited a protective effect on the steel. At the same time, the FZ near the IMC layer experienced intense corrosion; this was because of the galvanic corrosion between the FZ and IMC layer. The IMC layer was a cathode which accelerated the corrosion of Al and Zn in the FZ. There was slight corrosion of steel adjacent to the IMC layer, which was due to the IMC layer as the anode by an oxidation reaction protecting the steel from corrosion [41]. During the corrosion process of the Al/steel joints, Zn and Al in FZ and IMC were dissolved in large quantities to generate Zn^{2+} and Al^{3+} cations, and slight corrosion occured in the surface of steel that generated Fe^{3+} cations, which react with OH^- ions in the solution that generate products such as $Al(OH)_3$, $Zn(OH)_2$, and $Fe(OH)_3$ [42].
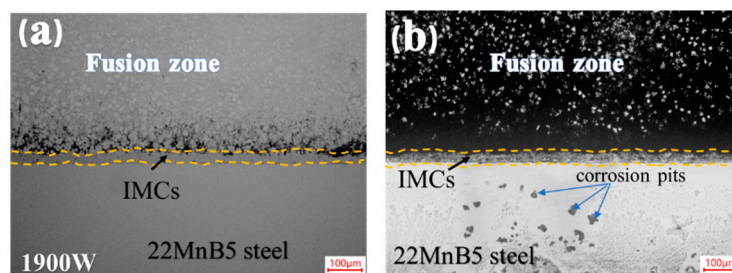

Figure 11. Interface morphology of Al/coated steel joints in 1900 W: (**a**) before corrosion, (**b**) after corrosion.
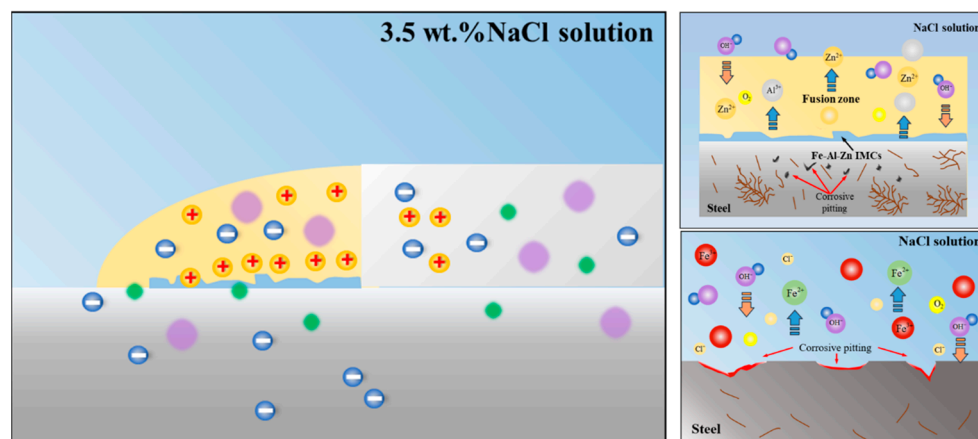

Figure 12. Schematic diagram of corrosion mechanism of Al/steel joints in 3.5% NaCl solution.

4. Conclusions

In this study, interfacial microstructures were observed, and electrochemical corrosion tests were designed to analyze the correlation between Al-Si coatings and corrosion resistance of aluminum/steel joints. The major research conclusions were as follows:

(1) In the Al/uncoated steel joints, $Fe_2Al_{5-x}Zn_x$ and $FeZn_{10}$ were generated at a laser power of 1500 to 1900 W; while, in the Al/Al-Si coated steel joints, pre-existing Fe_2Al_7Si within the Al-Si coating was observed at 1500 W, but $Fe_2Al_{5-x}Zn_x$ and $FeZn_{10}$ were detected while the laser power was 1700–1900 W.

(2) The Al-Si coating that consisted of Al-Si eutectic structure and Fe_2Al_7Si significantly depressed the formation and growth of the interfacial IMC layer because of the dual effects of thermal and diffusion barriers.

(3) The electrochemical corrosion tests indicated that the resistance to corrosion in Al/steel joints was noticeably enhanced by the Al-Si coating, specifically within the laser power range of 1700 to 1900 W, but had opposite effects on the joint corrosion resistance at 1500 W, which was mainly dictated by the thickness of interfacial IMCs layer.

(4) The galvanic corrosion that occurred between the FZ and the steel aggravated the corrosion process, while the galvanic corrosion between the FZ and IMC layer, the IMC layer as a cathode, accelerated the corrosion of the FZ; on the other hand, the galvanic corrosion between the steel and IMC layer, the IMC layer as the anode, protected the steel from corrosion.

Author Contributions: Writing—original draft, L.W.; conceptualization, F.W. and Y.Z.; methodology, J.P.O.; software, W.X.; validation, M.X. and M.Z.; formal analysis, J.P.O., Y.Z. and L.W.; investigation, M.Z. and W.X.; resources, H.Z. and J.Y.; data curation, L.W. and H.Z.; writing—review and editing, J.Y., J.P.O., F.W. and L.W.; visualization, M.X. and L.W.; supervision, H.Z.; funding acquisition, J.P.O. and J.Y. All authors have read and agreed to the published version of the manuscript.

Data Availability Statement: The raw data supporting the conclusions of this article will be made available by the authors on request.

Conflicts of Interest: The authors declare no conflicts of interest.

References

1. Kaushik, P.; Dwivedi, D.K. Al-steel dissimilar joining: Challenges and opportunities. *Mater. Today* **2022**, *62*, 6884–6899. [CrossRef]
2. Pouranvari, M.; Abbasi, M. Dissimilar gas tungsten arc weld-brazing of Al/steel using Al-Si filler metal: Microstructure and strengthening mechanisms. *J. Alloys Compd.* **2018**, *749*, 121–127. [CrossRef]
3. Torkamany, M.J.; Tahamtan, S.; Sabbaghzadeh, J. Dissimilar welding of carbon steel to 5754 aluminum alloy by Nd:YAG pulsed laser. *Mater. Des.* **2010**, *31*, 458–465. [CrossRef]
4. Kumar Deepati, A.; Alhazmi, W.; Benjeer, I. Mechanical characterization of AA5083 aluminum alloy welded using resistance spot welding for the lightweight automobile body fabrication. *Mater. Today* **2021**, *45*, 5139–5148. [CrossRef]
5. Zheng, M.; Yang, J.; Xu, J.Y.; Jiang, J.W.; Zhang, H.; Oliveira, J.P.; Lv, X.; Xue, J.; Li, Z. Interfacial microstructure and strengthening mechanism of dissimilar laser al/steel joint via a porous high entropy alloy coating. *J. Mater. Res. Technol.* **2023**, *23*, 3997–4011. [CrossRef]
6. Yang, L.; Wan, Y.; Qin, Z.; Xu, Q.; Min, Y. Fabrication and corrosion resistance of a graphene-tin oxide composite film on aluminium alloy 6061. *Corros. Sci.* **2018**, *130*, 85–94. [CrossRef]
7. Karbasian, H.; Tekkaya, A.E. A review on hot stamping. *J. Mater. Process. Technol.* **2010**, *210*, 2103–2118. [CrossRef]
8. Kügler, H.; Vollertsen, F. Inductive preheating in laser beam welding of multimaterial joints of 22MnB5 and AA6016. *Phys. Procedia* **2013**, *41*, 41–48. [CrossRef]
9. Kim, C.; Kang, M.J.; Park, Y.D. Laser welding of Al-Si coated hot stamping steel. *Pro. Eng.* **2011**, *10*, 2226–2231. [CrossRef]
10. Maggi, S.; Murgia, M. Introduction to the metallurgic characteristics of advanced high-strength steels for automobile applications. *Weld. Int.* **2008**, *22*, 610–618. [CrossRef]
11. Sun, Y.; Wu, L.; Tan, C.; Zhou, W.; Chen, B.; Song, X.; Zhao, H.; Feng, J. Influence of Al-Si coating on microstructure and mechanical properties of fiber laser welded 22MnB5 steel. *Opt. Laser Technol.* **2019**, *116*, 117–127. [CrossRef]
12. Lin, W.; Li, F.; Wu, D.; Chen, X.; Hua, X.; Pan, H. Effect of Al-Si Coating on Weld Microstructure and Properties of 22MnB5 Steel Joints for Hot Stamping. *J. Mater. Eng. Perform.* **2018**, *27*, 1825–1836. [CrossRef]
13. Ding, Y.; Shen, Z.; Gerlich, A.P. Refill friction stir spot welding of dissimilar aluminum alloy and AlSi coated steel. *J. Manuf. Process.* **2017**, *30*, 353–360. [CrossRef]
14. Zhang, K.; Wu, L.; Tan, C.; Sun, Y.; Chen, B.; Song, X. Influence of Al-Si coating on resistance spot welding of Mg to 22MnB5 boron steel. *J. Mater. Process. Technol.* **2019**, *271*, 23–35. [CrossRef]
15. Ma, H.; Qin, G.; Dang, Z.; Qu, S.; Chen, L.; Geng, P. Interfacial microstructure evolution and mechanical properties of inertia friction welded aluminium alloy/stainless steel joint with preheat treatment. *Mater. Sci. Eng. A* **2022**, *836*, 142671. [CrossRef]
16. Khalaj, G.; Moradi, M.; Asadian, E. Exploring the impact of rolling temperature on interface microstructure and mechanical properties of steel–bronze explosive welded bilayer composite sheets. *Weld. World* **2023**, *67*, 1411–1425. [CrossRef]
17. Ma, Y.; Dong, H.; Li, P.; Yang, J.; Wu, B.; Hao, X.; Xia, Y.; Qi, G. A novel corrosion transformation process in aluminum alloy/galvanized steel welded joint. *Corros. Sci.* **2022**, *194*, 109936. [CrossRef]
18. Jiang, J.; Oliveira, J.P.; Yang, J.; Zheng, M.; Li, H.; Xu, W.; Wu, L.; Dou, T.; Wang, R.; Tan, C.; et al. Effect of defocusing distance on interfacial reaction and mechanical properties of dissimilar laser Al/steel joints with a porous high entropy alloy coating. *Mater. Charact.* **2024**, *210*, 113751. [CrossRef]

19. Yang, J.; Oliveira, J.P.; Li, Y.; Tan, C.; Gao, C.; Zhao, Y.; Yu, Z. Laser techniques for dissimilar joining of aluminum alloys to steels: A critical review. *J. Mater. Process. Technol.* **2022**, *301*, 117443. [CrossRef]
20. Windmann, M.; Röttger, A.; Kügler, H.; Theisen, W. Microstructure and mechanical properties of the heat-affected zone in laser-welded/brazed steel 22MnB5–AA6016 aluminum/AZ31 magnesium alloy. *J. Mater. Process. Technol.* **2017**, *247*, 11–18. [CrossRef]
21. Narsimhachary, D.; Dutta, K.; Shariff, S.M.; Padmanabham, G.; Basu, A. Mechanical and microstructural characterization of laser weld-brazed AA6082-galvanized steel joint. *J. Mater. Process. Technol.* **2019**, *263*, 21–32. [CrossRef]
22. Yang, J.; Xiao, M.; Wu, L.; Li, Z.; Liu, H.; Zhao, Y.; Guo, W.; Tan, C. The influence of laser power on microstructure and properties of laser welding-brazing of Al alloys to Al-Si coated 22MnB5 steel. *Opt. Laser Technol.* **2023**, *162*, 109318. [CrossRef]
23. Cao, X.; Yi, Z.; Xu, C.; Luo, Z.; Duan, J.A. Study on laser/DP-MIG hybrid welding-brazing of aluminum to Al-Si coated boron steel. *J. Manuf. Process.* **2021**, *64*, 333–340. [CrossRef]
24. Cheng, W.-J.; Wang, C.-J. Microstructural evolution of intermetallic layer in hot-dipped aluminide mild steel with silicon addition. *Surf. Coat. Technol.* **2011**, *205*, 4726–4731. [CrossRef]
25. Windmann, M.; Röttger, A.; Kügler, H.; Theisen, W.; Vollertsen, F. Laser beam welding of aluminum to Al-base coated high-strength steel 22MnB5. *J. Mater. Process. Technol.* **2015**, *217*, 88–95. [CrossRef]
26. Gao, K.; Gu, H.; Gong, J.; Li, K.; Dai, X.; Ye, K. Microstructure and mechanical properties of induction rolling welded joint for A283GRC steel and 5052 aluminum alloy. *J. Mater. Process. Technol.* **2023**, *318*, 118016. [CrossRef]
27. Yu, G.; Chen, S.; Zhao, Z.; Wen, Z.; Huang, J.; Yang, J.; Chen, S. Comparative study of laser swelding-brazing of aluminum alloy to galvanized steel butted joints using five different filler wires. *Opt. Laser Technol.* **2022**, *147*, 107618. [CrossRef]
28. Jia, L.; Shichun, J.; Yan, S.; Cong, N.; Genzhe, H. Effects of zinc on the laser welding of an aluminum alloy and galvanized steel. *J. Mater. Process. Technol.* **2015**, *224*, 49–59. [CrossRef]
29. Ma, Y.; Dong, H.; Li, P.; Wu, B.; Huang, L.; Zhang, L.; Li, C.; Li, J. Galvanic corrosion of AA5052/304SS welded joint with Zn-based filler metal in marine engineering. *Corros. Sci.* **2023**, *211*, 110912. [CrossRef]
30. Ma, Y.; Dong, H.; Li, P.; Wu, B.; Wu, W.; Qian, W.; Wang, B. Control of various Zn-based weld seam/steel interface structures in AA5083/FH36 steel welded joint. *Mater. Des.* **2023**, *230*, 111971. [CrossRef]
31. El-Sayed, M.H.; Naka, M. Structure and properties of carbon steel–aluminium dissimilar joints. *Sci. Technol. Weld. Join.* **2013**, *10*, 27–31. [CrossRef]
32. Song, J.L.; Lin, S.B.; Yang, C.L.; Fan, C.L. Effects of Si additions on intermetallic compound layer of aluminum–steel TIG welding–brazing joint. *J. Alloys Compd.* **2009**, *488*, 217–222. [CrossRef]
33. Li, T.; Zhou, D.; Yan, Y.; Liu, J. Effect of beam oscillation on intermetallic compounds and mechanical properties of steel/aluminum laser welded joint. *J. Manuf. Processes* **2022**, *73*, 40–53. [CrossRef]
34. Bertoncello, J.C.B.; Manhabosco, S.M.; Dick, L.F.P. Corrosion study of the friction stir lap joint of AA7050-T76511 on AA2024-T3 using the scanning vibrating electrode technique. *Corros. Sci.* **2015**, *94*, 359–367. [CrossRef]
35. Wang, S.; Luo, K.; Sun, T.; Li, G.; Cui, J. Corrosion behavior and failure mechanism of electromagnetic pulse welded joints between galvanized steel and aluminum alloy sheets. *J. Manuf. Process.* **2021**, *64*, 937–947. [CrossRef]
36. Shi, Y.; Li, J.; Zhang, G.; Huang, J.; Gu, Y. Corrosion Behavior of Aluminum-Steel Weld-Brazing Joint. *J. Mater. Eng. Perform.* **2016**, *25*, 1916–1923. [CrossRef]
37. Volovitch, P.; Vu, T.N.; Allély, C.; Abdel Aal, A.; Ogle, K. Understanding corrosion via corrosion product characterization: II. Role of alloying elements in improving the corrosion resistance of Zn–Al–Mg coatings on steel. *Corros. Sci.* **2011**, *53*, 2437–2445. [CrossRef]
38. Rajabalizadeh, Z.; Seifzadeh, D. Application of electroless Ni-P coating on magnesium alloy via CrO3/HF free titanate pretreatment. *Appl. Surf. Sci.* **2017**, *422*, 696–709. [CrossRef]
39. Baek, J.S.; Kim, J.G.; Hur, D.H.; Kim, J.S. Anodic film properties determined by EIS and their relationship with caustic stress corrosion cracking of Alloy 600. *Corros. Sci.* **2003**, *45*, 983. [CrossRef]
40. Martins, C.M.B.; Moreira, J.L.; Martins, J.I. Corrosion in water supply pipe stainless steel 304 and a supply line of helium in stainless steel 316. *Eng. Fail. Anal.* **2014**, *39*, 65–71. [CrossRef]
41. Sravanthi, S.S.; Acharyya, S.G.; Joardar, J.; Chaitanya, V.N.S.K. A Study on Corrosion Resistance and Mechanical Performance of 6061 Aluminium Alloy: Galvanized Mild Steel Electron Beam Welds at Varying Welding Parameters. *Trans. Indian Inst. Met.* **2020**, *73*, 881–895. [CrossRef]
42. Liu, W.; Li, M.C.; Luo, Q.; Fan, H.Q.; Zhang, J.Y. Influence of alloyed magnesium on the microstructure and long-term corrosion behavior of hot-dip Al–Zn–Si coating in NaCl solution. *Corros. Sci.* **2016**, *104*, 217–226. [CrossRef]